Article type: Research paper

Nitrogen-carbon graphite-like semiconductor synthesized from uric acid

Roberto C. Dante[1*], Pedro Chamorro-Posada[2], José Vázquez-Cabo[3], Óscar Rubiños-López[3], Francisco M. Sánchez-Árevalo[4], Lázaro Huerta[4], Pablo Martín-Ramos[5], Luis Lartundo-Rojas[6], Carlos F. Ávila-Vega[7], Edgar D. Rivera-Tapia[8], Cristian A. Fajardo-Pruna[9], Álvaro J. Ávila-Vega[10] and Omar Solorza-Feria[11]

[1] Research, Development & Innovation, 2Dto3D S.r.l.s. Via Revalanca 5, 12036 San Firmino, Revello (CN), Italy.

[2] Dpto. de Teoría de la Señal y Comunicaciones e IT, Universidad de Valladolid, ETSI Telecomunicación, Paseo Belén 15, 47011 Valladolid, Spain.

[3] Dpto. de Teoría de la Señal y Comunicaciones, Universidad de Vigo, ETSI Telecomunicación, Lagoas Marcosende s/n, Vigo, Spain.

[4] Instituto de Investigaciones en Materiales, Universidad Nacional Autónoma de México, Apdo. Postal 70-360, Cd. Universitaria, Mexico City 04510, Mexico.

[5] EPS, Instituto Universitario de Ciencias Ambientales de Aragón (IUCA), Universidad de Zaragoza, Carretera de Cuarte s/n, 22071, Huesca, Spain.

[6] Instituto Politécnico Nacional, Centro de Nanociencias y Micro y Nanotecnologías de Nanociencias, UPALM, Zacatenco, Mexico City, 07738, Mexico.

[7] Departamento de Ingeniería Civil y Ambiental, Escuela Politécnica, Escuela Politécnica Nacional (EPN), Ladrón de Guevara E11 - 253. Quito, Ecuador.

[8] Newcastle University, School of Mechanical Engineering, Newcastle upon Tyne NE1

[*] Corresponding author. Tel: +39 3407536757. E-mail: rcdante@yahoo.com

7RU, UK.

[9] Escuela Politécnica Nacional, Departamento de Formación Básica, Ladrón de Guevara E11-253 Quito, Ecuador.

[10] Instituto Nacional de Eficiencia Energética y Energías Renovables (INER), Iñaquito N3537 y Juan Pablo Saenz, Quito, Ecuador.

[11] Departamento de Química, Centro de Investigación y de Estudios Avanzados del Instituto Politécnico Nacional (CINVESTAV-IPN). Av. IPN 2508, Col. San Pedro Zacatenco, Apdo. Postal 14-740, Mexico D.F. 07360, Mexico.

Abstract

A new carbon-nitrogen organic semiconductor has been synthesized by pyrolysis of uric acid. This layered carbon-nitrogen material contains imidazole-, pyridine (naphthyridine)- and graphitic-like nitrogen, as evinced by infrared and X-ray photoelectron spectroscopies. Quantum chemistry calculations support that it would consist of a 2D polymeric material held together by hydrogen bonds. Layers are stacked with an interplanar distance between 3.30 and 3.36 Å, as in graphite and coke. Terahertz spectroscopy shows a behavior similar to that of amorphous carbons, such as coke, with non-interacting layers. This material features substantial differences from polymeric carbon nitride, with some characteristics closer to those of nitrogen-doped graphene, in spite of its higher nitrogen content. The direct optical band gap, dependent on the polycondensation temperature, ranges from 2.10 to 2.32 eV. Although in general the degree of crystallinity is low, in the material synthesized at 600 °C some spots with a certain degree of crystallinity can be found.

Keywords: carbon nitride, nitrogen-carbon materials, organic semiconductor, THz

spectroscopy, uric acid

1. Introduction

The piece of work presented herein on the products obtained from the pyrolysis of uric acid (UA) started with the objective to find an alternative pathway for the synthesis of polymeric carbon nitride (g-C_3N_4), an organic semiconductor that is receiving substantial attention due to its versatility and many potential applications [1-15]. However, the chosen precursor yielded a material with a lower nitrogen content (N to C atomic ratio ~0.6) than that of g-C_3N_4 (N to C atomic ratio of 1.33) and different polymer structure and electronic properties.

This novel carbon-nitrogen material would also belong to the class of organic semiconductors, which combine the electronic advantages of semiconducting materials with the chemical (and mechanical) benefits of organic compounds. Therefore, the ability to absorb light and conduct electricity is coupled with a structure with a flexible backbone that can easily be modified by chemical synthesis (however, the control of modifications would depend on several factors).

The new synthesized material can be regarded as a graphitic material with imidazole-, pyridine (naphthyridine)- and graphitic-like nitrogen. Nonetheless, whereas the concentration of nitrogen in the either nitrogen-doped or defective graphite is around 2 or 3 at% (N to C atomic ratio of *ca*. 0.03), the nitrogen content in this new material is much higher (~33 at%), forcing to a less randomized distribution of defects. For example, the recently synthesized C_2N exhibited a very organized 2D structure. C_2N, in combination with g-C_3N_4, offers a potential way to improve the efficiencies of both photoabsorption and electron–hole separation of g-C_3N_4 without involving any transition metals. Fechler *et al*. synthesized nitrogen rich graphitic materials starting from various

types of quinones and urea as precursors, showing that the amount of nitrogen in the final materials depended on reaction temperature [16-19].

Another extensively nitrogen-doped (mesoporous) carbon was synthesized by Goel *et al.* from melamine and formaldehyde. They obtained an interesting cross-linked structure by nanocasting that would mainly be ascribed to a certain type of melamine-formaldehyde resin with a high content of bridging oxygen atoms [20]. On the contrary, the material under study has a very low content of oxygen. Organic semiconductors of the indolocarbazole family have similar nitrogen-containing basic units and tend to have a π-π stacking and band gaps between 2.50 and 2.90 eV, depending on the side chains and the oligomer type [21-23]. Their degree of crystallinity has been shown to depend largely on the side chains and oligomer length, copolymers, as well as on the deposition method [21,22]. When they are part of large polymers, they tend to be more amorphous and the diffraction peaks become much broader and can be considerably shifted [23]. An example of these basic semiconductors is shown in Fig. 1, where R can be a side chain.

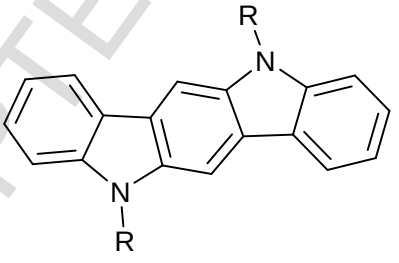

Fig. 1. Chemical structure of based oligomers, R is a side chain [22].

The specific combination of imidazolic, pyridinic, and graphitic nitrogen of the materials synthesized with UA is actually determined by the decomposition pathway of the crystalline UA and can be regarded as one of the upper limits of nitrogen-doped graphite (graphene) materials, such as those reported by Fechler, Zussblatt, Rothe,

Schlögl, Willinger, Chmelka and Antonietti [19] and Mahmood Mahmood, Lee, Jung, Shin, Jeon, Jung, Choi, Seo, Bae, Sohn, Park, Oh, Shin and Baek [17].

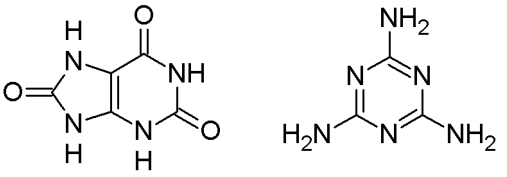

Fig. 2. Chemical structures of uric acid (*left*) and melamine (*right*).

2. Experimental

2.1. *Materials*

Uric acid was supplied by Aesar and melamine was supplied by Sigma-Aldrich with purities higher than 99% (the chemical formulas are displayed in Fig. 2). A mixture of 95 wt% of uric acid and 5 wt% of melamine was prepared and milled in an agate mortar for 5 min (both materials are solids). Portions of 5 g of the blend were treated at different temperatures and times in air: 450 °C for 15 min, 550 °C for 15 min, 600 °C for 15 and 30 min. Samples were identified as CN450, CN550, CN600-1, and CN600-2, respectively. The (weight) reaction yields were 74.33%, 67.87%, 44.89%, and 34.36%, respectively, corresponding to different decomposition advancements and to the formation of nitrogen-rich powder products. The products exhibited different colors, ranging from brown (CN450) to intense black (CN600-2).

2.2. *Analytical methods*

FT-IR spectroscopy: The infrarred spectra were acquired by means of a Agilent Carey 630 Fourier Transform-Infrarred (FT-IR) spectrometer (Agilent Technologies, Santa Clara, CA, USA). The IR spectra were obtained directly from the solid materials by attenuated total reflectance (ATR).

X-ray diffraction measurements: The X-ray diffraction patterns were obtained with a Rigaku ULTIMA-IV Bragg-Brentano powder diffractometer (Rigaki Corp., Tokyo, Japan) with Cu Kα radiation. Glass capillaries were used for sample mounting. The measurements always lasted for 1 hour, and crystalline silicon was used as a standard.

TEM characterization: Samples were studied by transmission electron microscopy (TEM) with a JEM-2010F and a JEM-1010 (JEOL, Akishima, Tokyo, Japan) in order to observe the particles morphology at lower magnifications and to find structural information complementary to the X-ray diffraction data. The samples' preparation consisted in dispersing the materials into 2-butanol, treating them in an ultrasonic bath for 30 min, and then depositing a micro-droplet (2.5μL) of the suspended fraction on a Cu grid. Once the 2-butanol evaporated, the grids were ready for observation.

Thermal analysis: The thermal stability and decompostion rate of the products was evaluated by thermogravimetric analysis using a SETSYS Evolution 1750 TGA-DTA/DSC (SETARAM Instrumentation, Caluire-et-Cuire, France) with an nitrogen flow rate of 30 mL/min and a temperature increment rate of 10 °C/min up to 900 °C.

UV-vis spectroscopy: UV-Vis diffuse reflectance spectra were measured using a Perkin Elmer Lambda 35 UV-Vis spectrophotometer (Perkin Elmer Inc., Waltham, MA, USA). A Spectralon® blank was used as reference. The reflectance data were transformed to absorbance data applying the Kubelka-Munk method (Equation 1):

$$F(R) = \frac{(1 - R)^2}{2R} \quad (1)$$

where R is the reflectance and $F(R)$ is the Kubelka-Munk (K-M) function. The band gap was estimated through a Tauc plot [24,25].

TeraHertz-time domain spectroscopy measurements: The materials under study were dispersed in polyethylene (PE) powder in a variable low concentration and the mixture was thoroughly ground in an agate mortar in order to form a uniform mixture. Ultra-high

molecular weight surface-modified, 53–75 μm particle size PE from Sigma–Aldrich was employed. The resulting samples were pressed, using a Graseby Specac press, to form pellets with a diameter of 13 mm. A Menlo Tera K15 Spectrometer (Menlo Systems GmbH, Planegg, Germany) was used for the THz-TDS analysis. The system was operated in a nitrogen rich atmosphere in order to avoid the signature of water absorption in the recorded samples. In order to reduce the noise, the results from at least twenty consecutive samples and reference measurements were averaged to obtain the spectral data. The material parameters in the spectral range of interest were calculated from the time domain photocurrent traces measured with the spectrometer. These time domain waveforms depend not only on the material data but also on the width of the pellets due to the contributions from multiple reflections at the pellet-air interfaces. Signal processing techniques similar to those described by Duvillaret *et al*. and flat-top windowing of the time-domain data were employed in order to obtain the THz spectra of the materials [26,27].

X-ray photoelectron spectroscopy: X-ray photoelectron spectroscopy (XPS) analyses were performed using a Versa Probe II X-ray photoelectron spectrometer (Physical Electronics, Chanhassen, MN, USA) with a monochromatic Al Kα X-ray source (1486.6 eV) and a base pressure of 1×10^{-9} Torr in the analytical chamber. The X-rays were microfocused at the source to give a spot size on the sample of 100 μm in diameter, using the standard-lens mode. The analyzer was run in constant analyzer energy (CAE) mode. Survey and high resolution spectra were collected using analyzer pass energies of 120 and 40 eV, respectively. The binding energy of 284.6 eV of C-C carbon was used as a reference and as a starting point for the C1s peak deconvolution. High resolution spectra were deconvoluted using Gaussian–Lorentzian mix function and Shirley-type background subtraction.

Quantum chemistry calculations: The semiempirical quantum chemistry computations were performed with the PM6 method using the parallel implementation for multi-threaded shared-memory CPUs and massively parallel GPU acceleration of the MOPAC2012 software package. A Fedora Linux server with a 12 cores Intel Xeon processor and a NVIDIA Tesla K20 GPU were used for the computations [28-30].

3. Results and discussion

3.1. *Structural and physical-chemical characterization*

3.1.1. *Infrared spectroscopy*

The IR spectrum of solid UA (see Fig. 3) was dominated by the absorptions related to three chemical groups: NH, OH, and carbonyl CO. The amidic carbonyl generates two bands at 1650 and 1580 cm^{-1}, typical of secondary amides; the band at 1477 cm^{-1} can be related to C-OH bending; and the broad band at around 3000 cm^{-1} is connected to OH stretching vibrations, all interacting by hydrogen bond. The observation of vibrations associated with OH, instead of only CO, is due to imide-amide tautomerism. The imide form of uric acid would be predominant in this supramolecular solid, held by hydrogen bonds. The series of bands between 1410 and 1300 cm^{-1} can be ascribed to O-H in-plane bending vibrations, while the vibration of out-of-plane bending is located at 680 cm^{-1}. The two main peaks between 1123 and 983 cm^{-1} correspond to C-O stretching vibrations of COH. The peaks at 874 and 780 cm^{-1} are due to N-H bending and N-H wagging, respectively.

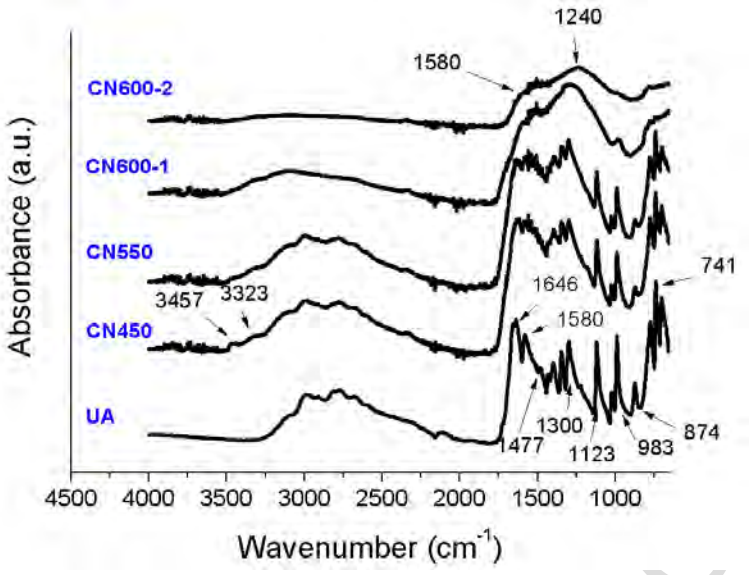

Fig. 3. IR spectra of uric acid (UA) and its pyrolysis products obtained at 450 °C, 550 °C and 600 °C: CN450, CN550, CN600-1 and CN600-2 (CN600-1: 15 min of treatment, CN600-2: 30 min of treatment).

The spectrum of CN450 showed the same bands discussed for the UA starting material. However, it was possible to notice that some small bands appeared at 3457 and 3323 cm^{-1}. These new bands correspond to OH stretching vibrations not interacting via hydrogen bond, and so they would be indicative of the beginning of the disaggregation of the supramolecular network. Moreover, the bands of carbonyl stretching and those of OH in-plane bending seemed to be overlapped with two new growing broad bands. The situation for CN550 was similar, since the forming pyrolysis product was mixed with the initial UA and their bands were still overlapped. This transition phase is supported by the appearance of free OH stretching vibration from the remaining UA molecules, which are no longer interacting via hydrogen bond due to the transformation of their UA neighbors into the pyrolysis products.

The situation radically changed in CN600-1 and CN600-2 spectra, in which most bands associated to OH, CO and NH groups disappeared. In the spectrum of the former,

some residual C-OH bands were still present, such as the small peak at around 983 cm^{-1}. A shoulder due to carbonyl stretching could also be discerned above 1600 cm^{-1}. It is worth noting that the stretching bands of non-interacting OH (above 3300 cm^{-1}) were proportionally higher than those of CN450 and CN550 samples, indicating that the pyrolysis process was more advanced. Conversely, in CN600-2 spectrum the OH stretching bands had almost disappeared. The broad bands at 1580 and 1240 cm^{-1} seem to be associated to vibrations of 6-5 atoms nitrogen-containing rings [31-33]. Indeed, the band at 1580 cm^{-1} may belong to ring stretching vibrations from both pyridine-like and imidazole (or pyrrole) -like rings, while the band at 1240 cm^{-1} can be associated to C-N stretching of imidazole-like rings [34]. This latter claim is also supported by the similarity of the spectrum of CN600-2 to that of nitrogen-doped graphene, where pyrrole-like and pyridine-like nitrogen atoms are present, apart from graphitic nitrogen [32,33,35].

3.1.2. *Morphology of the products: TEM analysis*

TEM micrographs, representative of the suspended fraction (see Section 2.2) of each of the pyrolysis products, are depicted in Fig. 4.

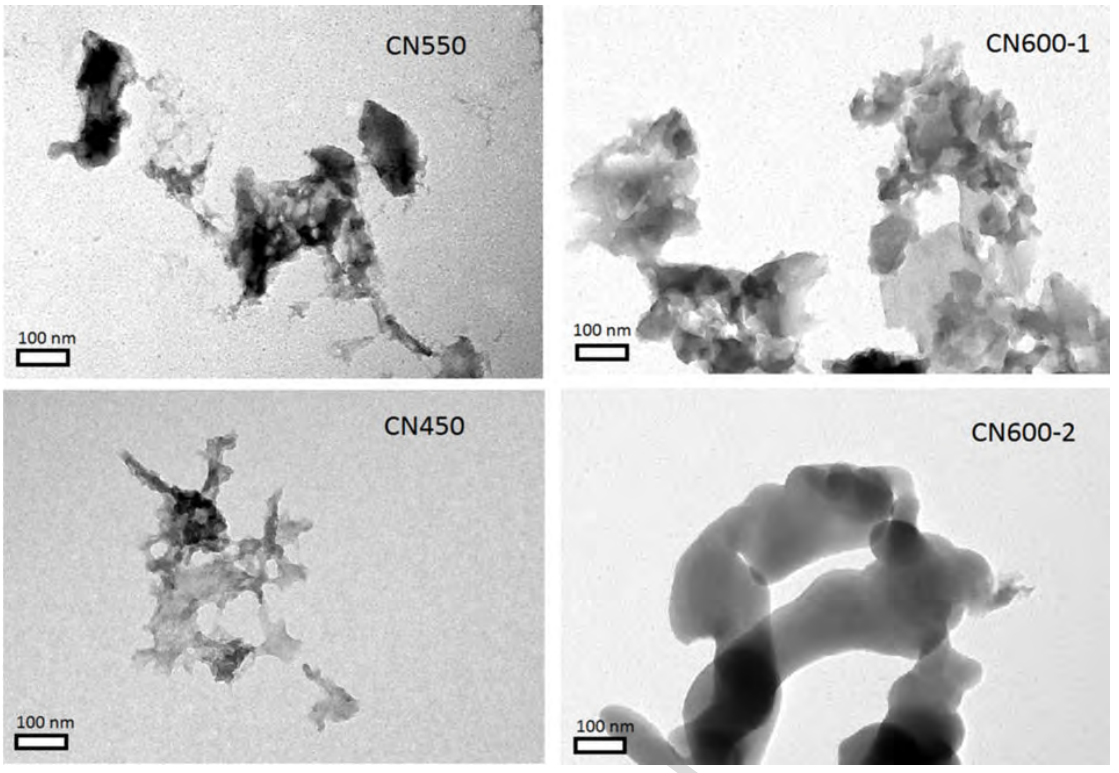

Fig. 4. TEM micrographs of CN450, CN550, CN600-1 and CN600-2.

It is noteworthy that the morphology of CN450, with crumpled particles, was similar to that observed in the formation of g-C_3N_4 from melamine cyanurate, which occurs through a topotactic transformation [36]. In CN550 and CN600-1 samples the particles were mainly composed of nanosheets, while in CN600-2 these nanosheets also tended to form hollow structures, as a consequence of the topotactic transformation advancement. As regards CN600-2 sample, it was possible to observe diffraction planes in certain more ordered spots (see Fig. 5). The interplanar distance, 3.36 Å, was found to be compatible with the main peak in the XRD pattern.

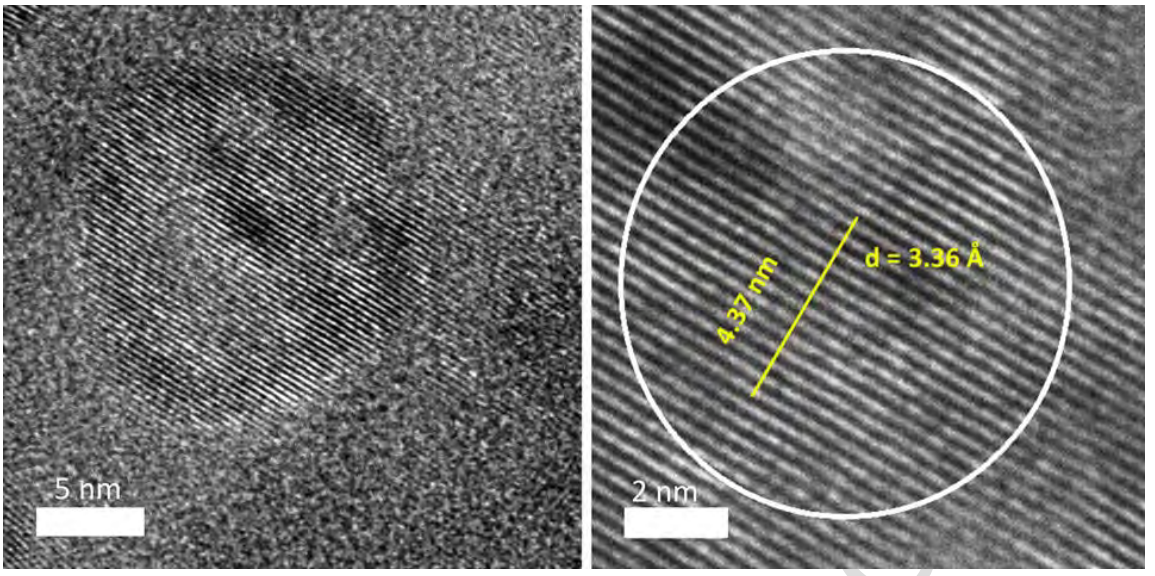

Fig. 5. Diffraction planes in TEM micrographs of CN600-2 sample. *left*: a view on a particle showing an ordered spot in the middle of a more disordered area; *right*: zoomed view of the ordered spot.

3.1.3. *X-ray diffraction (XRD) measurements*

The powder X-ray diffraction patterns of CN450 and CN550 samples, shown in Fig. 6, were in agreement with that of crystalline UA. This further supports that the starting material (UA) would be still present in considerable amounts in samples treated below 600 °C (the XRD pattern of CN450 was almost identical to that of anhydrous uric acid) [37]. Moreover, the XRD pattern of CN600-1 corresponded to a quite amorphous material with a broad peak around 27°, which seems to result directly from the UA peak at 27°, provided that the basic layered features of the original structure would be preserved (topotactic transformation). Nevertheless, all the other peaks were not visible. The intensity of the reflection at 26.97°, corresponding to an interplanar spacing of 3.31 Å, became much higher and the peak remained quite broad, while the broad peak at 12.58° (spacing of 7.03 Å), corresponding to an in-plane structural packing motif, became more evident. It should be pointed out that in the final product the stacking order

seems to prevail over the in-plane one. The crystallization process driven by temperature was also revealed by the broad exothermic band found in differential scanning calorimetry at *ca*. 600 °C.

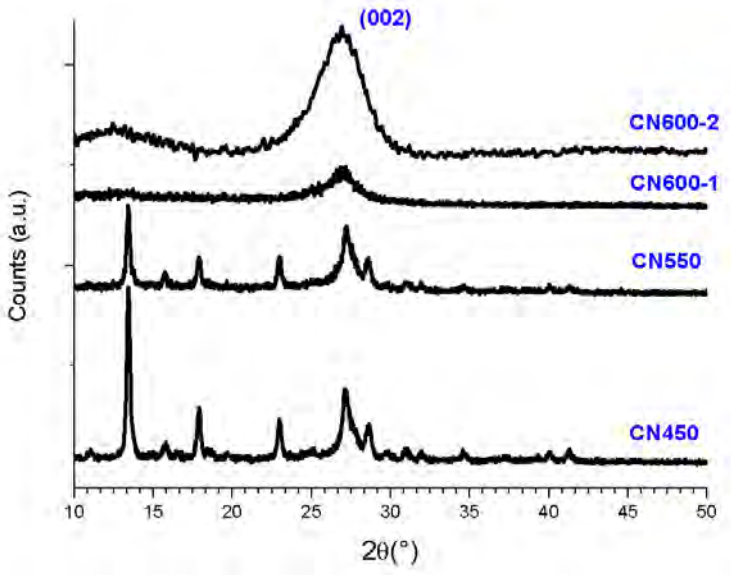

Fig. 6. X-ray diffraction patterns of CN450, CN550, CN600-1, and CN600-2.

The typical diffraction peak at around 27° has also been found in other nitrogen-doped graphene or graphite materials. In fact, Horibe *et al*. reported that this interplanar distance decreases monotonously with increasing N/C content ratio [38,39]. According to Horibe's reports, an interplanar distance of 3.31 Å would correspond to an N/C atomic ratio close to 0.6, which is actually very close to the one found by X-ray photoelectron spectroscopy for the materials under study.

3.1.4. *Thermal behavior analysis*

The weight losses in the thermogravimetric analysis (TGA) curves of both CN450 and CN550 samples (see Fig. 7) in nitrogen atmosphere above 400 °C can be ascribed to UA and melamine decomposition. The loss at around 400 °C (first circle in the TGA

thermograms in Fig. 7) was more pronounced in CN450 than in CN550 because of the higher starting material concentration in the former (in which polycondensation was conducted at a lower temperature). These losses were no longer present in CN600-1 and CN600-2 samples, indicating that in the both cases UA had been completely consumed. The second weight loss above 600 °C (second circle in Fig. 7), present in all samples, was due to the final decomposition of the products.

The endothermic peaks in the differential thermal calorimetry (DSC) curves of both CN450 and CN550 (see inset in Fig. 7) at around 400 °C can thus be associated to the starting materials' decomposition. Other DSC peaks above 600 °C may be due to the decomposition of by-products in CN450. The endothermic peaks around 400 °C were no longer present in CN600-1 and CN600-2. On the contrary, broad exothermic peaks at around 600 °C appeared in both CN600-1 and CN600-2 (especially evident in CN600-2). It seems that, in conjunction with the final (endothermic) decomposition, a (exothermic) process of crystallization occurred. These processes were eventually confirmed by X-ray diffraction.

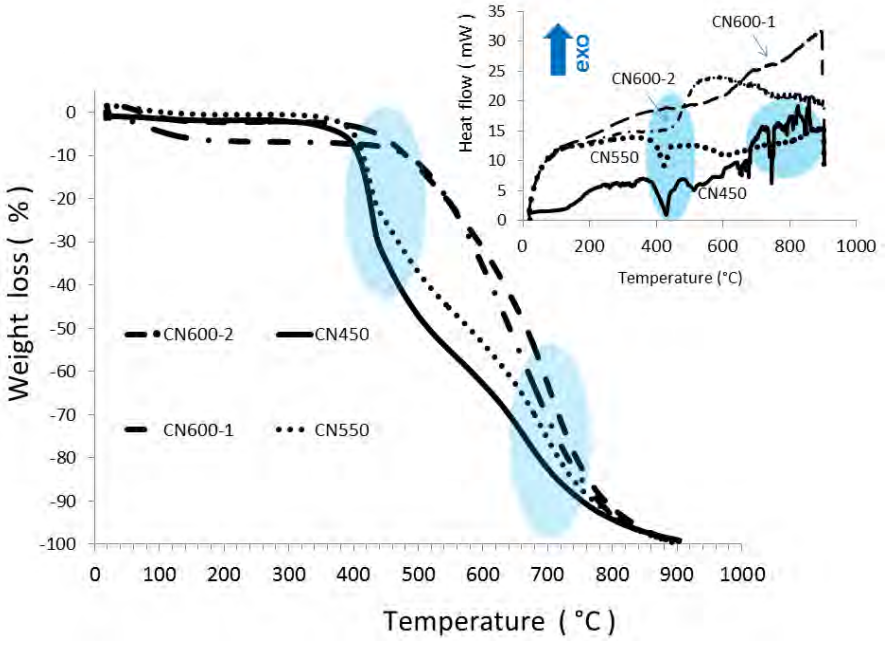

Fig. 7. Thermogravimetric curves of CN450, CN550, CN600-1, and CN600-2. *Inset*: differential scanning calorimetry curves of the same samples. The circles in the graphics highlight the main transformations.

3.1.5. *UV-visible spectroscopy*

The UV-visible spectra of the four samples exhibited an increase in the absorption as the polycondensation temperature was increased, as shown in Fig. 8. In the spectrum of CN600-2 there was an evident but broad peak between 1.7 and 1.5 eV (around the wavelength of 750 nm) in the red region. The increment in this band intensity would correspond to the enrichment of the samples in final product as a function of the thermal treatment temperature, also confirmed by other techniques.

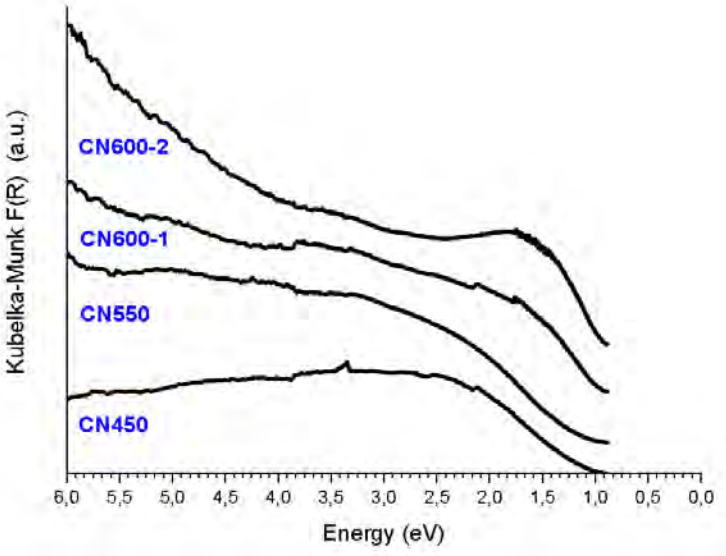

Fig. 8. UV-visible Kubelka-Munk, *F(R)*, spectra of CN450, CN550, CN600-1, and CN600-2.

The direct band gap values estimated by Tauc plot were 2.10, 2.22 and 2.32 eV for CN550, CN600-1 and CN600-2, respectively. The direct band gap could not be

determined by Tauc plot for CN450, since the final product yield was still low in this case. Moreover, the indirect band gap was considerably lower and had values around 0.90 eV for all the samples, indicating that this gap is more related to the assembly of the product molecules.

3.1.6. *X-ray photoelectron spectroscopy*

In order to confirm the incorporation of nitrogen atoms into the polymer network and to identify the carbon-nitrogen species formed during the synthesis process, XPS analysis of the four semiconducting polymer samples was conducted. The evolution and quantification of the carbon, nitrogen and oxygen species was established by comparison of the relative intensities of the C1s, N1s and O1s peaks (Fig. 9) and by elemental quantification of the carbon, nitrogen and oxygen contents (Table 1).

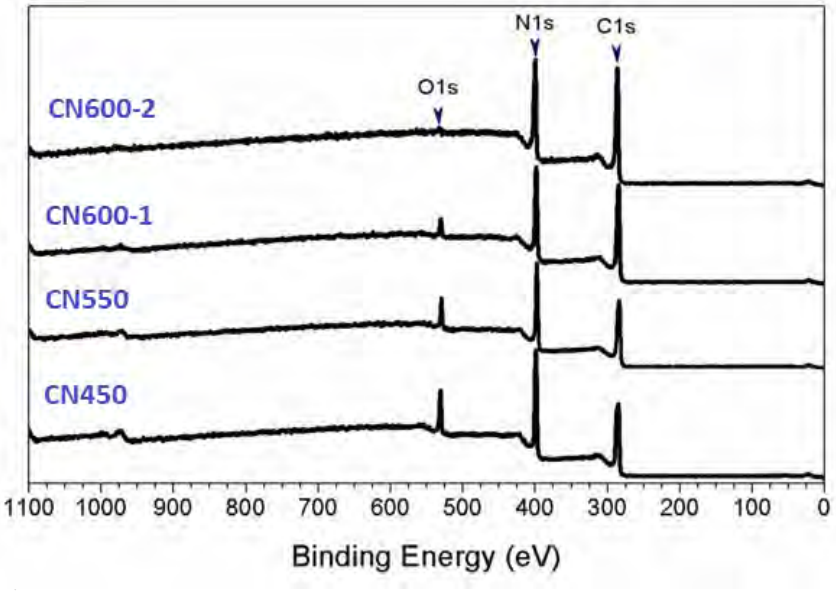

Fig. 9. XPS survey spectra of the samples CN450, CN550, CN600-1, and CN600-2.

Table 1. Estimated elemental carbon, nitrogen and oxygen contents for the different UA polycondensation products.

Sample	C [%]	N [%]	O [%]
CN450	52.4	36.1	11.5
CN550	55.3	34.4	10.3
CN600-1	56.3	36.7	7.0
CN600-2	58.2	37.4	4.4

The high-resolution XPS spectra in the C1s region of the four samples are shown in Fig. 10. The spectra were fitted by six Gaussian-Lorentzian contributions with binding energies (BE) centered at 284.8, 285.8, 286.9, 288.1, 289.1 and 291.6 ±0.2 eV, and corresponding to C-C and sp^2 (C=C) (C1), pyridinic (naphthyridinic) C-N (C2), C=O and imidazolic C-N-H (C3), -COOH and imidazolic C=N (C4), O-C(=O)-O (C5) and π-π* (C6), respectively [40-46]. The binding energies and relative weight percent (wt%) associated with each contribution are summarized in Table 2.

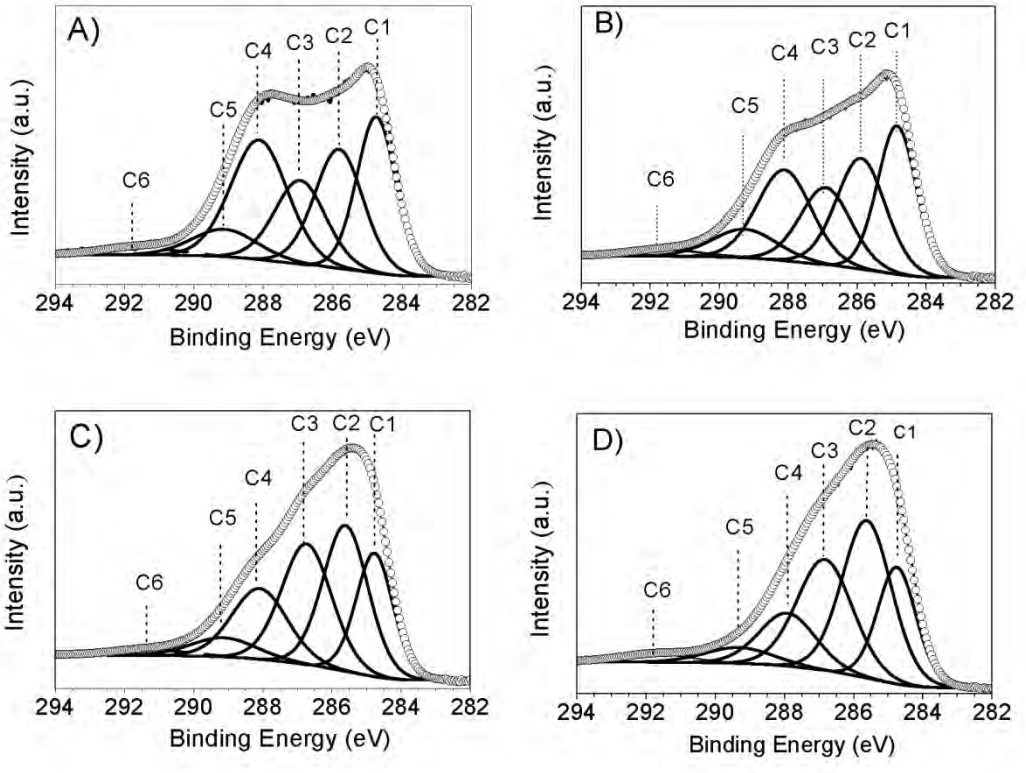

Fig. 10. High-resolution XPS spectra in the C1s region: deconvoluted peaks for the

various UA polycondensation products: A) CN450, B) CN550, C) CN600-1 and D) CN600-2.

Table 2. Deconvolution and carbon chemical species quantification results for C1s core level spectra (BE: binding energies).

Sample		C1	C2	C3	C4	C5	C6
BE	BE [± 0.2 eV]	284.8	285.8	286.9	288.1	289.1	291.6
CN450	wt%	24.2	22.8	16.9	26.8	7.1	2.3
CN550	wt%	25.8	24.4	17.6	21.9	8.3	2.1
CN600-1	wt%	20.0	29.0	26.6	17.2	5.5	1.9
CN600-2	wt%	19.5	33.8	26.7	12.9	4.7	2.4

The presence of five nitrogen species in the N1s region, 395.0–407.0 eV, was verified upon deconvolution of the high-resolution spectra of the four samples under study (see Fig. 11). The BEs of the five Gaussian-Lorentzian contributions (*viz*. 398.3, 399.1, 400.2 and 404.2 ±0.2 eV), corresponding to pyridinic (naphthyridinic) N (N1), imidazolic C-NH (N2) (a small part of N2 can be also due to nitrile species, since a very weak peak can be seen in the IR spectrum of CN600-2), imidazolic C-N-C (N3), graphitic N (i.e. a 3-coordinated N similar to that of amorphous CN_x) or C-O-N (N4), and π-π* (N5), respectively [39-45], and relative weight percent (wt%) values are presented in Table 3.

The ratio N1:N2:N3 for CN600-2 was approximately 1:1:1, suggesting that these types of nitrogen could belong to a well-defined structure (not randomly distributed). It is noteworthy that imidazole seems to be formed before than naphthyridine (in fact, the N2 and N3 contents were higher than those of N1 in the samples treated below 600 °C), which implies the condensation of the 6 atoms-rings of two UA molecules.

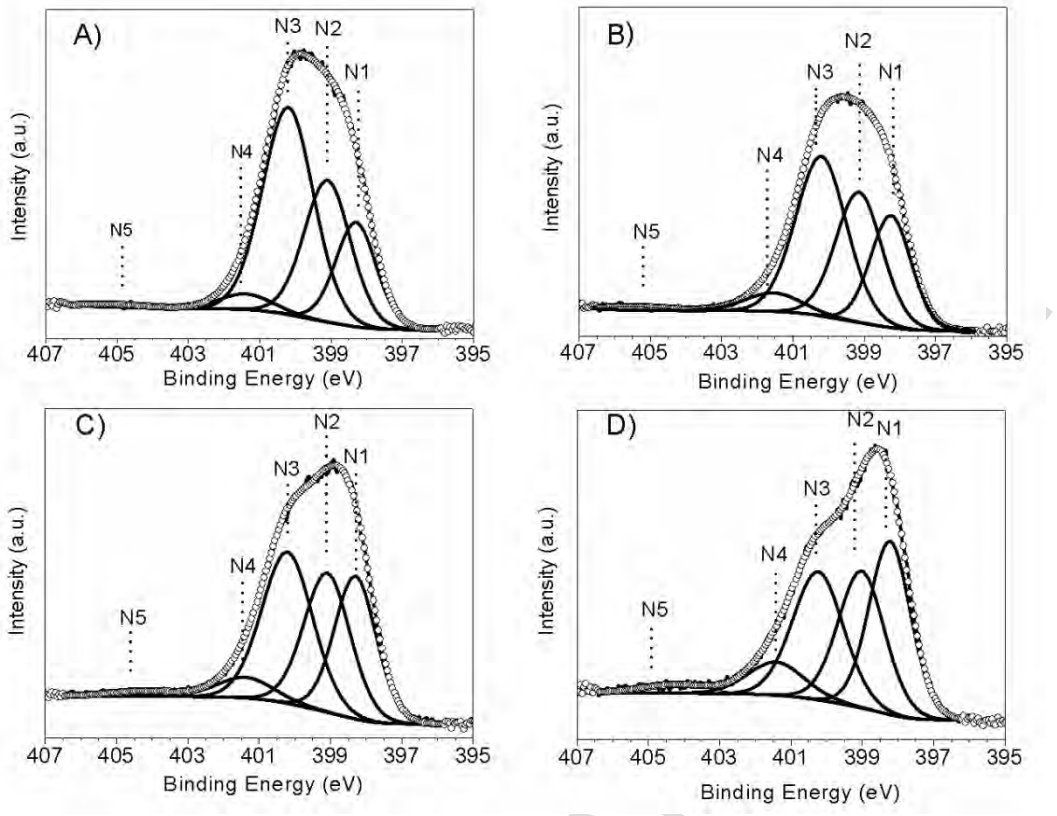

Fig. 11. High-resolution XPS spectra in the N1s region: deconvoluted peaks for the various UA polycondensation products: A) CN450, B) CN550, C) CN600-1 and D) CN600-2.

Table 3. Deconvolution and nitrogen chemical species quantification results for N1s core level spectra (a) BE was 404.2 eV for both CN600-1 and CN600-2.

Sample		N1	N2	N3	N4	N5
BE	BE [± 0.2 eV]	398.3	399.1	400.2	401.4	405.0
CN450	wt%	19.0	29.4	47.0	3.8	0.8
CN550	wt%	22.8	30.2	40.5	5.3	1.3
CN600-1	wt%	27.6	29.8	35.5	5.4	1.7(a)
CN600-2	wt%	31.9	28.2	28.9	8.4	2.6(a)

The O1s peaks (in the 529.0–537.0 eV region), arising from the oxygen-carbon species or from water absorbed on the surface of the semiconductor polymers, are depicted in Fig. 12, together with their fit to three Gaussian-Lorentzian contributions. These contributions, centered at 531.8, 532.5 and 534.2 ± 0.2 eV, were correlated with

372 N-C-O (O1), C-O or C-OH (O2) and adsorbed H_2O (O3), respectively. The oxygen
373 bonds and their relative mass fractions (wt%) are condensed in Table 4.

374

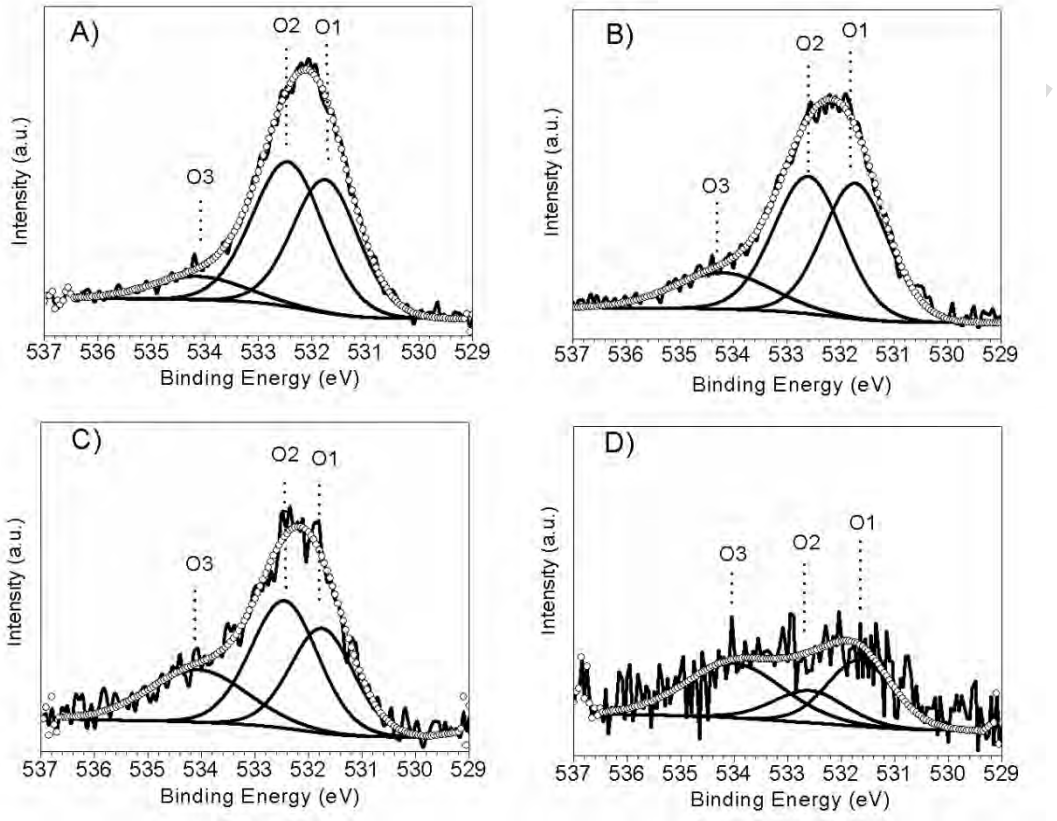

375

376 **Fig. 12.** High-resolution XPS spectra in the O1s region: deconvoluted peaks for the
377 various UA polycondensation products: A) CN450, B) CN550, C) CN600-1 and D)
378 CN600-2.

379

380 **Table 4.** Deconvolution and oxygen chemical species quantification results for O1s core
381 level spectra(BE: binding energies).

Sample		O1	O2	O3
BE	BE [± 0.2 eV]	531.8	532.5	534.1
CN450	wt%	41.2	48.6	10.3
CN550	wt%	40.3	43.4	16.3
CN600-1	wt%	32.5	42.3	25.2
CN600-2	wt%	36.3	19.3	44.5

382

383

3.1.7. *THz-TDS measurements*

The room temperature THz-TDS spectra of the four pyrolysis products in the 0.8–2.2 THz range are shown in Fig. 13(a) displays the results for pure material pellets –except for CN600-2, which was diluted at a 45 wt% concentration in a PE matrix (since it was impossible to prepare a pure sample pellet)–, while Fig. 13(b) shows the spectra for all the samples dispersed in PE at a 20 wt% concentration. Even though the total absorption was much smaller in this case, which made the measurements noisier, it provided a fair comparison between all the samples.

Previously reported THz-TDS measurements of UA at 77 K showed two peaks in this band: a very strong resonance close to 1.5 THz and a much smaller peak near 1.35 THz [47]. Both peaks were clearly present in the UA and CN550 samples, in particular the strongest absorption band, albeit with a red-shift of both resonances, as they were measured at room temperature. This temperature dependence is typical of THz vibrational resonances associated with crystal lattice modes [48]. In the present case, the main signature of the THz spectrum was shifted to 1.44 THz when the measurement was performed at room temperature. A contribution to the total attenuation –that increased monotonically with frequency– was present, which would be due to scattering. There was also a small absorption band at 1.99 THz, which can be due to the presence of melamine at a small concentration [49].

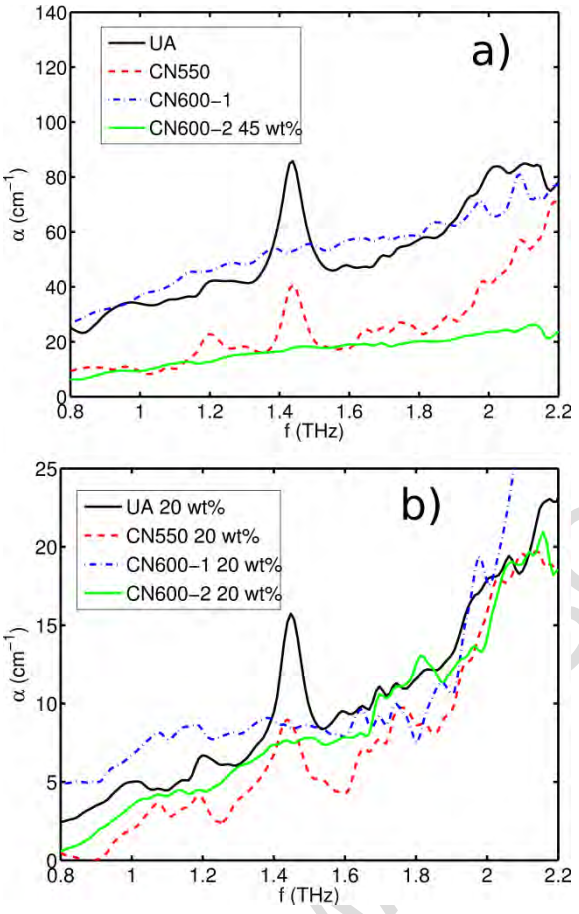

404

405 **Fig. 13.** THz-TDS measurements of the samples. The results in (a) correspond to pure
406 samples, except for CN600-2, for which a pellet in a PE matrix with 45 wt% was used.
407 In (b), all the samples were dispersed at a 20 wt% concentration in PE.

408

409 The significant reduction of the signature contributed by the precursor material to the
410 total attenuation after thermal treatment at 550 ºC indicates its transformation into the
411 carbon-nitrogen product. When the processing temperature was further increased to 600
412 ºC, the attenuation traces of the reagent completely disappeared and the attenuation
413 features typical of disordered materials dominated [50]. There was a reduction of the
414 total attenuation of CN600-2 when compared to that of CN600-1. Also, the faint
415 resonance in the higher frequency end of the spectrum that was common to the CN550
416 and CN600-1 samples vanished in CN600-2. In spite of the fact that the observed
417 spectral peak was very weak, the THz spectra can be interpreted as an effect of the initial

production of the 2D polymer, supporting its presence at an appreciable concentration in CN550 and CN600-1 samples. This conformation has a lattice mode that has been calculated at 2.28 THz and a stronger resonance at 3.23 THz (see below). The presence of this type of lattice resonances in a disordered material can contribute to the generation of a broad spectral feature similar to that observed in CN600-1, and the reduction of the attenuation can indicate a progressive condensation of the material into the 3D phase (stacking of layers) [51]. A similar transition has also been previously explained for g-C_3N_4 on the basis of THz-TDS measurements [52].

3.2. *Semi-empirical quantum chemistry calculations*

3.2.1. *Geometry optimization*

Uric acid crystals are monoclinic with four molecules in a unit cell (Fig. 14), with parameters a=14.464 Å, b=7.403 Å, c=6.208 Å, β=65.10^o [53]. The crystal geometry was optimized with these parameters as the initial conditions using the PM6 method and periodic boundary conditions. The computational period spanned 1×2×3 crystal unit cells in the *a*, *b*, and *c* directions, respectively, in order to fulfill the accuracy requirements of MOPAC calculations [54].

The crystal parameters of the geometry optimized with the PM6 Hamiltonian were a=14.870 Å, b=7.307 Å, c=6.401 Å, α=89.76^o, β=64.67^o and γ=89.78^o, very close to their actual values. In these conditions, it can be expected that the vibrations predicted in the THz range will be close to those of the measured data [48,55].

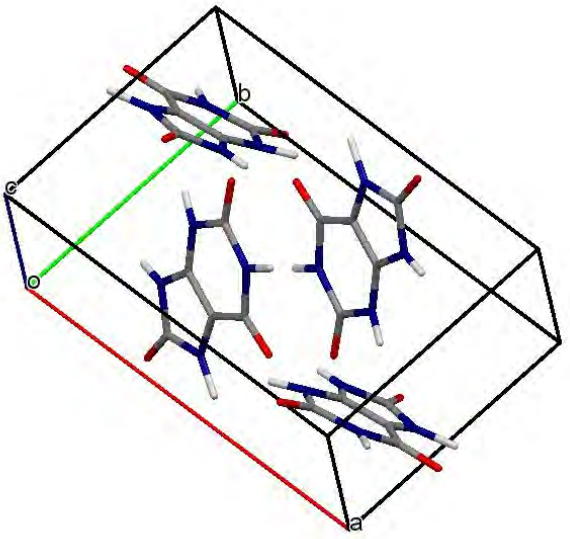

Fig. 14. Unit cell of uric acid.

Fig. 15 shows the optimized geometry corresponding to the new carbon-nitrogen material, consistent with the observed elemental ratio by XPS. It consists of an alternating sequence of imidazole and naphthyridine units resulting in a material with an average formula of $C_5N_3H_2$ (with an atomic ratio of nitrogen to carbon of 0.6), which would be formed by condensation of uric acid molecules, as indicated in Equation 2:

$$2nC_5H_4N_4O_3 \rightarrow (C_{10}N_6H_4)_n + 2nH_2O + 2nNO_2 \quad (2)$$

In the polymer unit, shown in Fig. 15, the ratio of N1:N2:N3 is 1:1:1, as determined by XPS. The experimental ratio of N to C of 0.64 for the CN600-2 product, as determined by XPS, could be ascribed to the presence of a certain amount of graphitic nitrogen (a nitrogen bonded to three carbon atoms in the naphthenic ring) as a defect in the polymer chain with three N atoms in the naphthenic rings. Indeed, the N to C ratio becomes 0.6 when such graphitic nitrogen is neglected.

The calculations were performed with the PM6 Hamiltonian and periodic boundary conditions using MOPAC. The length of the polymer repeat unit was a=10.353 Å. In spite of the large polarity of imidazole, the symmetric combination of two constituents

of this type in the polymer repeat unit permits to cancel out the dipole moment. PM6 calculations using MOPAC assign a dipole moment of 4.083 D and 2.772x10^{-3} D to the imidazole molecule and to the monomer of the carbon-nitrogen system, respectively.

Fig. 16 shows the resulting geometry for a 2D polymer obtained by the arrangement of linear chains linked by hydrogen bonds, in a similar fashion to those linking the linear polymer chains in the 2D melon system [52]. The lattice parameters for the 2D polymer were a=10.360 Å, b=6.251 Å and γ=89.25º. Both the 1D and 2D polymers would have a very good planarity.

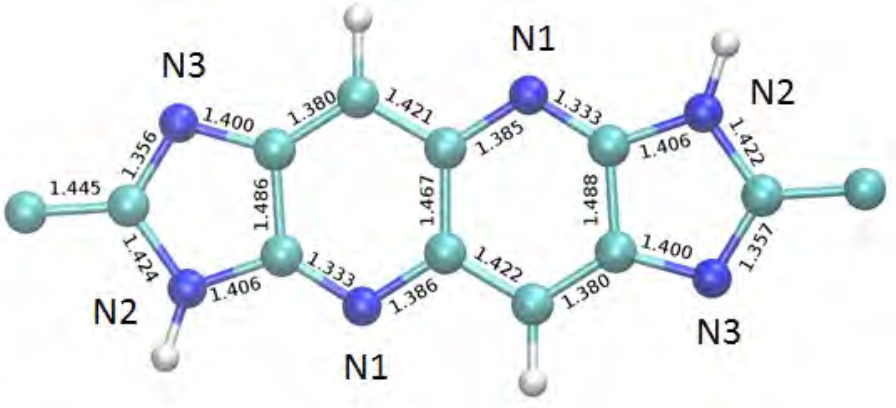

Fig. 15. Optimized geometry for the 1D polymer using the PM6 Hamiltonian. Bond lengths (in Å) are labeled in the figure. N1, N2, and N3 correspond to the nitrogen types identified by XPS. The N1:N2:N3 ratio is 1:1:1, as determined by XPS.

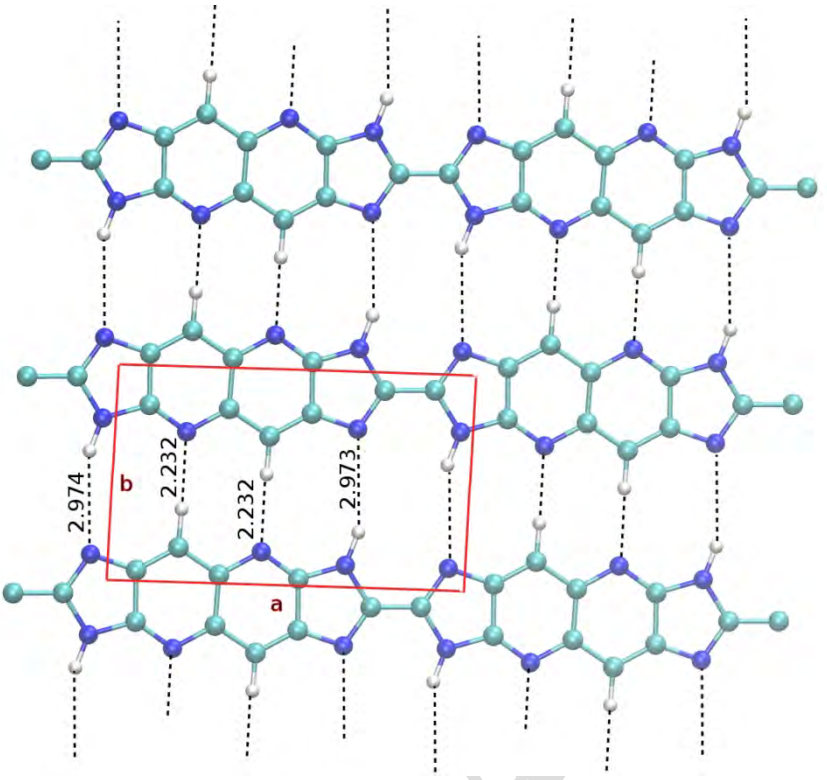

Fig. 16. Optimized geometry for the 2D polymer using the PM6 Hamiltonian. Hydrogen bonds linking the 1D chains are shown with dotted lines. Interatomic distances are in Å.

The optimized geometry of the 3D crystal obtained with the PM6 method is shown in Fig. 17. The corresponding lattice parameters were a=10.358 Å, b=6.280 Å, c=6.928 Å, α=85.09º, β=93.69 º and γ=89.61 º. The comparison of these results with those of the 2D geometry shows that the 3D geometry would be constituted by piled-up 2D polymer layers which would remain essentially undistorted. The inter-layer distance would be d=3.451 Å, in reasonable agreement with the experimental value.

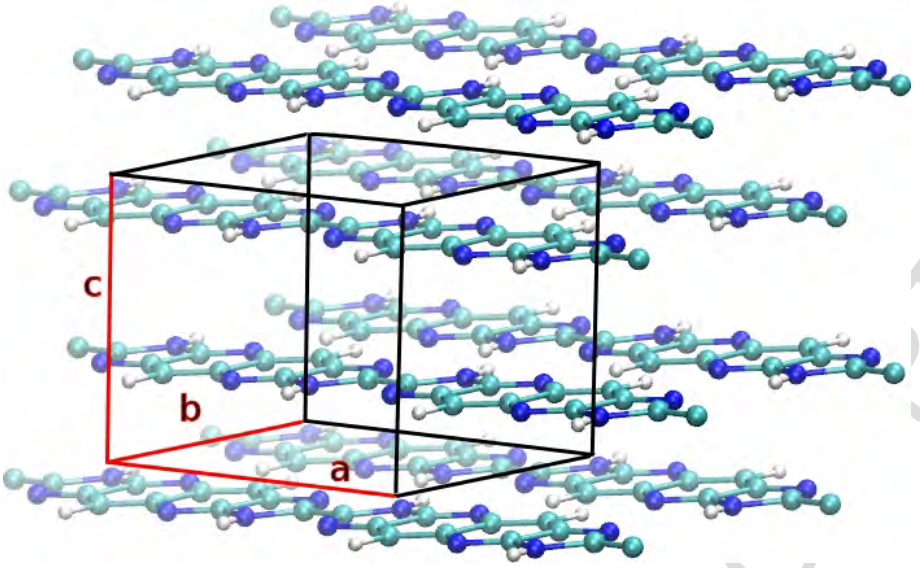

Fig. 17. Optimized geometry for the 3D arrangement obtained from the stacking of 2D polymer layers using the PM6 Hamiltonian.

The comparison of the XRD pattern simulated from the PM6 geometry with that experimentally measured for CN600-2, using Mercury software, is shown in Fig. 18 [54]. There is a small shift of the peak at 2θ=25.84° due to reflections at consecutive material stacks when compared with the corresponding signal in the XRD measurements that is consistent with the previously calculated value of *d*. The peak at 2θ=14.14° is also identified in the XRD measurements and can be attributed to reflection at every-other layer. This is a characteristic feature (with varying relative intensity) of related ABAB stacked carbon-nitrogen materials [52].

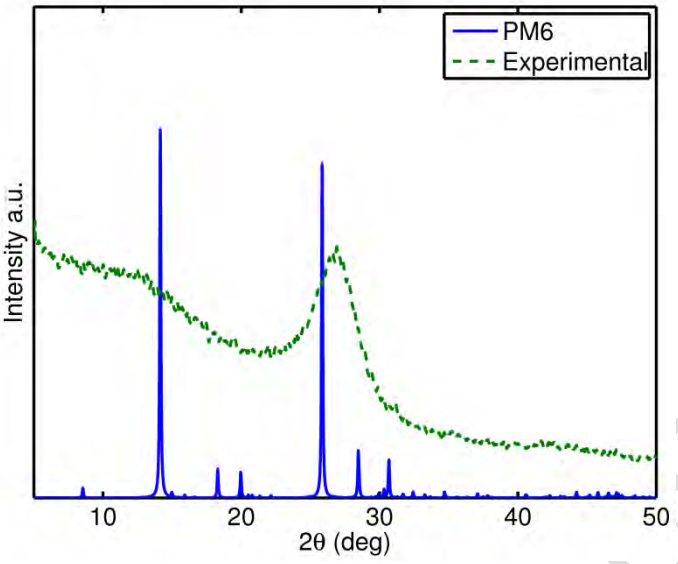

Fig. 18. Simulated X-ray powder diffraction pattern for the geometry optimized with the PM6 Hamiltonian shown in Fig. 17 (*solid line*) and experimental pattern for CN600-2 sample (*dotted line*).

The total energies per $C_{10}H_4N_6$ unit of the 1D polymer, 2D polymer and 3D crystal for the geometries optimized with the PM6 Hamiltonian were -2353.83538 eV, -2354.07442 eV, and -2354.19016 eV, respectively, thus indicating that the condensation sequence from the 1D to the 2D and, from there, to the 3D phase would be an energetically favorable process.

3.2.2. *Vibrational analysis*

As discussed above, the study of periodic structures using MOPAC requires an extended computational period spanning several crystal cells such that the size is sufficient for an accurate calculation [55]. This has the effect that the calculated frequencies are not limited to those fulfilling the condition k≈0 that permits the conservation of total momentum in the interaction with photons and that, therefore, are relevant for the absorption spectrum. Thus, a requirement in the interpretation of the MOPAC

calculations of vibration modes in periodic systems is the selection of the relevant vibrations from the whole set of calculated modes [48,56].

All the optimized geometries in this study corresponded to true ground states, except for the 3D system depicted in Fig. 17, for which it was not possible to obtain a geometry free from imaginary frequency vibrations.

All the plots of displacements of vibration modes were produced with Gabedit [57]. In each case, the atomic displacements were scaled to facilitate their visualization.

The atomic displacements associated to the main resonance of uric acid in the THz band are shown in Fig. 19. This mode was calculated at 1.41 THz, in excellent accordance with the THz-TDS measurements, as expected from the good correspondence between the calculated and experimental crystal parameters.

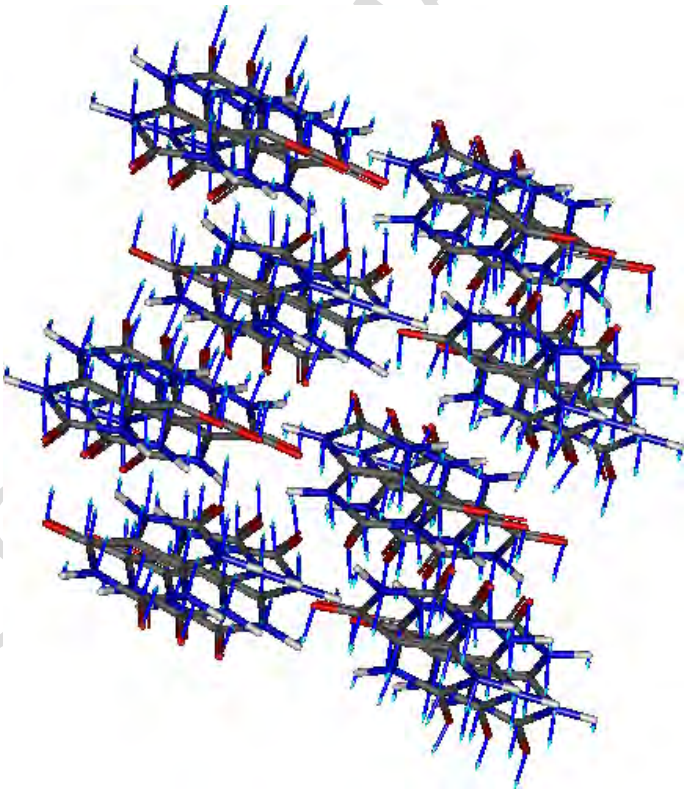

Fig. 19. Atomic displacements for the main vibration mode in the THz band calculated at 1.41 THz with the PM6 method using MOPAC.

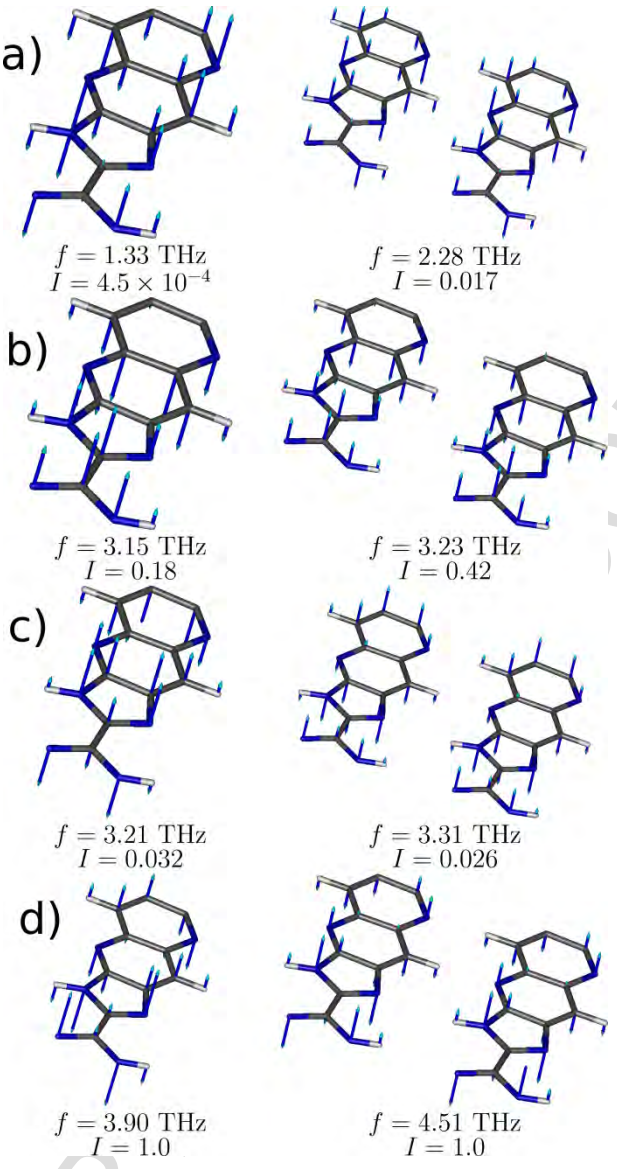

Fig. 20. Atomic displacements for the lowest k=0 vibration modes of the 1D (left) and 2D (right) polymers. The calculated vibration frequencies *f* and relative values of transition dipoles *I* are annotated in the plot.

Fig. 20 displays the lowest k≈0 vibration mode calculated for the 1D (left) and 2D (right) polymers in the spectral region ranging from 0 up to 6 THz. The side by side comparison of the plots shows that there exists a direct correspondence between the vibration modes of the 1D and 2D polymers, even though some differences in the

resonance frequencies and relative intensities can be appreciated. The main vibrations in this band correspond to modes b and d in Fig. 20, at 3.15 THz (3.23 THz) and 3.90 THz (4.51 THz) for the 1D (2D) carbon-nitrogen polymer, respectively.

As commented above, these vibrations may play a key role in the interpretation of the THz-TDS measurements for labeling the changes in the material morphology for different processing conditions.

3.2.3. *Band gap calculation*

Whether a polymer has a direct or indirect band gap can often be predicted from the nodal pseudo-symmetries of the HOMO and LUMO of the constituent monomer at the connecting atomic sites [58]. In this case, such a simple approach is not possible because the monomer HOMO is a non-bonding orbital with nulls at the connecting sites. The electronic band structure calculated using MOPAC, depicted in Fig. 21(a), shows a direct band gap at the edge of the Brillouin zone. Also, the very low dispersive character of the valence band, consistent with the properties of the HOMO, can be appreciated. Besides, the stacking along the *c* axis, can produce the appearance of an indirect band gap in the 3D conformation [58].

Even though solid-state MNDO calculations provide a good qualitative description of the band structure of materials, the quantitative estimates of the band gap can be largely biased, in contrast with the high predictive power of vibrational resonances of this type of methods. On the other hand, the bandgap of a polymer can be estimated with good accuracy using the INDO/S with configuration interaction singles (CIS) [59] by the extrapolation of the first excited state obtained for finite size oligomers as the chain length *n* grows [60]. The periodic 1D geometry optimized with the PM6 method implemented in MOPAC was used to generate oligomer geometries of several orders.

The energy of the first excited state in each case was calculated using the INDO/S-CIS method, implemented in the ORCA software package [61,62]. The results for the calculated energies for the *n*-mers are shown in Fig. 21(b) as a function of the inverse chain length 1/*n*, together with their corresponding least squares linear fit, which permits to extrapolate the value of E_g as 2.35 eV. This is in very good agreement with the experimental measurements.

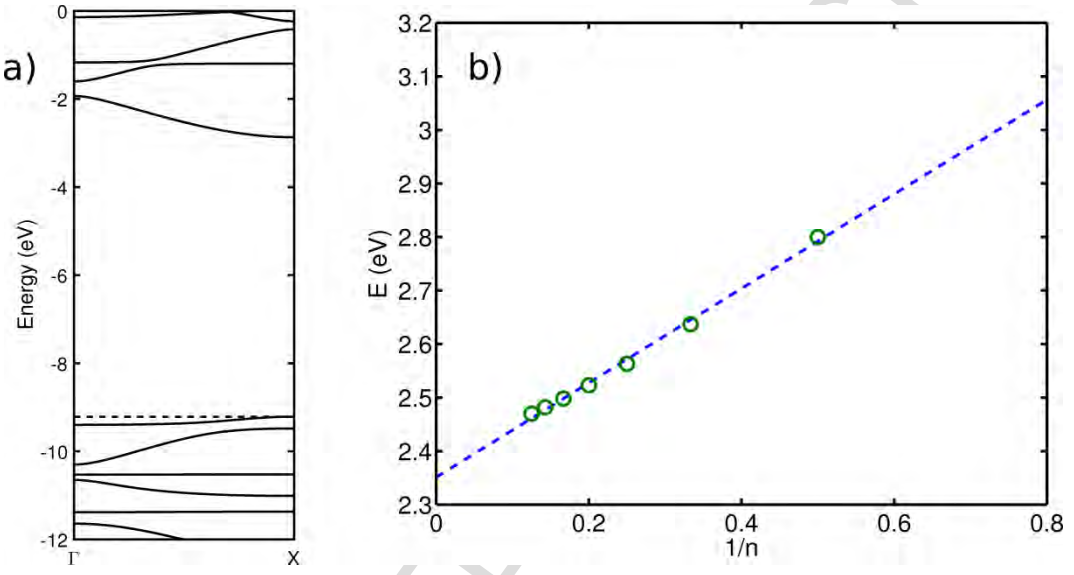

Fig. 21. (a) Band structure of the 1D polymer calculated using MOPAC. The Fermi level is indicated with a dashed line. (b) Energies for the *n*-mers calculated with INDO/S-CIS as a function of the inverse chain length 1/*n*, together with their corresponding least squares linear fit.

4. Conclusions

A new 2D carbon-nitrogen material was synthesized by pyrolysis of uric acid. The experimental results, obtained through XPS and vibrational spectroscopies, and the quantum chemistry simulations suggest that it would consist in a polymer containing imidazole-like and pyridine (naphthyridine)-like units, held together by a network of

hydrogen bonds. This organic semiconductor exhibits characteristics which substantially differ from those of g-C_3N_4, and can be regarded as one of the upper-limit cases of nitrogen-doped graphite (graphene), featuring an atomic ratio of nitrogen to carbon close to 0.6, corresponding to a formula of C_5N_3. The experimental ratio was 0.64 because of the presence of a certain amount of graphitic nitrogen as a defect in the polymer chain. The amount of this type of 3-coordinated nitrogen (possibly belonging to amorphous CN_x species) increased in the samples synthesized at 600 °C, and can be subject of further studies. Its direct optical band gap ranged from 2.10 to 2.32 eV, depending on the polycondensation temperature, very close to the experimental value of 2.35 eV obtained from semiempirical calculations. This band gap is lower than that of g-C_3N_4, allowing this new material to absorb more visible light with a view to its application as a photocatalyst. A good correspondence between experimental and calculated values was also attained for the interplanar distance (*ca*. 3.31 Å), which was consistent with a topotactic transformation, and for the THz-TDS spectroscopy spectra, which showed a behavior similar to that of amorphous 2D carbons, with non-interacting layer planes.

References

[1] M.L. Cohen, Calculation of bulk moduli of diamond and zinc-blende solids, Phys. Rev. B 32(12) (1985) 7988-7991.

[2] A.Y. Liu, M.L. Cohen, Structural properties and electronic structure of low-compressibility materials: β-Si_3N_4 and hypothetical β-C_3N_4, Phys. Rev. B 41(15) (1990) 10727-10734.

[3] X. Li, J. Zhang, L. Shen, Y. Ma, W. Lei, Q. Cui, et al., Preparation and characterization of graphitic carbon nitride through pyrolysis of melamine, Appl. Phys. A 94(2) (2008) 387-392.

608 [4] Y. Zhao, Z. Liu, W. Chu, L. Song, Z. Zhang, D. Yu, et al., Large-Scale Synthesis
609 of Nitrogen-Rich Carbon Nitride Microfibers by Using Graphitic Carbon Nitride
610 as Precursor, Adv. Mater. 20(9) (2008) 1777-1781.
611 [5] R.C. Dante, J. Martín-Gil, L. Pallavidino, F. Geobaldo, Synthesis under Pressure
612 of Potential Precursors of CNx Materials Based on Melamine and Phenolic Resins,
613 J. Macromol. Sci., Part B: Phys. 49(2) (2010) 371-382.
614 [6] G. Zhang, M. Zhang, X. Ye, X. Qiu, S. Lin, X. Wang, Iodine Modified Carbon
615 Nitride Semiconductors as Visible Light Photocatalysts for Hydrogen Evolution,
616 Adv. Mater. 26(5) (2014) 805-809.
617 [7] J. Zhang, J. Sun, K. Maeda, K. Domen, P. Liu, M. Antonietti, et al., Sulfur-
618 mediated synthesis of carbon nitride: Band-gap engineering and improved
619 functions for photocatalysis, Energy Environm. Sci. 4(3) (2011) 675.
620 [8] Y. Zhang, X. Bo, A. Nsabimana, C. Luhana, G. Wang, H. Wang, et al., Fabrication
621 of 2D ordered mesoporous carbon nitride and its use as electrochemical sensing
622 platform for H_2O_2, nitrobenzene, and NADH detection, Biosens. Bioelectron. 53
623 (2014) 250-256.
624 [9] Y. Zhang, T. Mori, J. Ye, Polymeric Carbon Nitrides: Semiconducting Properties
625 and Emerging Applications in Photocatalysis and Photoelectrochemical Energy
626 Conversion, Sci. Adv. Mater. 4(2) (2012) 282-291.
627 [10] Y. Zhang, Z. Schnepp, J. Cao, S. Ouyang, Y. Li, J. Ye, et al., Biopolymer-
628 Activated Graphitic Carbon Nitride towards a Sustainable Photocathode Material,
629 Sci. Rep. 3 (2013).
630 [11] A. Vinu, K. Ariga, T. Mori, T. Nakanishi, S. Hishita, D. Golberg, et al.,
631 Preparation and Characterization of Well-Ordered Hexagonal Mesoporous Carbon
632 Nitride, Adv. Mater. 17(13) (2005) 1648-1652.

[12] H. Zhao, M. Lei, X.a. Yang, J. Jian, X. Chen, Route to GaN and VN Assisted by Carbothermal Reduction Process, J. Am. Chem. Soc. 127(45) (2005) 15722-15723.

[13] J.L. Zimmerman, R. Williams, V.N. Khabashesku, J.L. Margrave, Synthesis of Spherical Carbon Nitride Nanostructures, Nano Lett. 1(12) (2001) 731-734.

[14] C. Cao, F. Huang, C. Cao, J. Li, H. Zhu, Synthesis of Carbon Nitride Nanotubes via a Catalytic-Assembly Solvothermal Route, Chem. Mater. 16(25) (2004) 5213-5215.

[15] A. Thomas, A. Fischer, F. Goettmann, M. Antonietti, J.-O. Müller, R. Schlögl, et al., Graphitic carbon nitride materials: variation of structure and morphology and their use as metal-free catalysts, J. Mater. Chem. 18(41) (2008) 4893.

[16] D. Wei, Y. Liu, Y. Wang, H. Zhang, L. Huang, G. Yu, Synthesis of N-Doped Graphene by Chemical Vapor Deposition and Its Electrical Properties, Nano Lett. 9(5) (2009) 1752-1758.

[17] J. Mahmood, E.K. Lee, M. Jung, D. Shin, I.-Y. Jeon, S.-M. Jung, et al., Nitrogenated holey two-dimensional structures, Nat. Commun. 6 (2015) 6486.

[18] H. Wang, X. Li, J. Yang, The g-C_3N_4/C_2N Nanocomposite: A g-C_3N_4-Based Water-Splitting Photocatalyst with Enhanced Energy Efficiency, ChemPhysChem 17(13) (2016) 2100-2104.

[19] N. Fechler, N.P. Zussblatt, R. Rothe, R. Schlögl, M.-G. Willinger, B.F. Chmelka, et al., Eutectic Syntheses of Graphitic Carbon with High Pyrazinic Nitrogen Content, Adv. Mater. 28(6) (2016) 1287-1294.

[20] C. Goel, H. Bhunia, P.K. Bajpai, Mesoporous carbon adsorbents from melamine–formaldehyde resin using nanocasting technique for CO_2 adsorption, J. Environ. Sci. 32 (2015) 238-248.

[21] Y. Wu, Y. Li, S. Gardner, B.S. Ong, Indolo[3,2-b]carbazole-Based Thin-Film Transistors with High Mobility and Stability, J. Am. Chem. Soc. 127(2) (2005) 614-618.

[22] P.-L.T. Boudreault, S. Wakim, N. Blouin, M. Simard, C. Tessier, Y. Tao, et al., Synthesis, Characterization, and Application of Indolo[3,2-b]carbazole Semiconductors, J. Am. Chem. Soc. 129(29) (2007) 9125-9136.

[23] M. Akimoto, T. Kawano, Y. Iwasawa, Y. Takahashi, K. Yamashita, M. Kawamoto, et al., Syntheses and properties of copolymers containing indolocarbazole moiety in the side chain, Polym. J. 43(12) (2011) 959-965.

[24] J. Tauc, R. Grigorovici, A. Vancu, Optical Properties and Electronic Structure of Amorphous Germanium, Physica Status Solidi B: Basic Solid State Physics 15(2) (1966) 627-637.

[25] J. Tauc, Optical properties and electronic structure of amorphous Ge and Si, Mater. Res. Bull. 3(1) (1968) 37-46.

[26] L. Duvillaret, F. Garet, J.L. Coutaz, A reliable method for extraction of material parameters in terahertz time-domain spectroscopy, IEEE J. Sel. Top. Quantum Electron. 2(3) (1996) 739-746.

[27] J. Vázquez-Cabo, P. Chamorro-Posada, F.J. Fraile-Peláez, Ó. Rubiños-López, J.M. López-Santos, P. Martín-Ramos, Windowing of THz time-domain spectroscopy signals: A study based on lactose, Opt. Commun. 366 (2016) 386-396.

[28] J.J.P. Stewart, Optimization of parameters for semiempirical methods V: Modification of NDDO approximations and application to 70 elements, J. Mol. Model. 13(12) (2007) 1173-1213.

[29] J.D.C. Maia, G.A. Urquiza Carvalho, C.P. Mangueira, S.R. Santana, L.A.F. Cabral, G.B. Rocha, GPU Linear Algebra Libraries and GPGPU Programming for

683 Accelerating MOPAC Semiempirical Quantum Chemistry Calculations, J. Chem.
684 Theory Comput. 8(9) (2012) 3072-3081.
685 [30] J.J.P. Stewart, MOPAC2012, Stewart Computational Chemistry, Colorado
686 Springs, CO, USA, 2012.
687 [31] I. López Tocón, M.S. Woolley, J.C. Otero, J.I. Marcos, Vibrational spectrum of 3-
688 methyl and 4-methylpyridine, J. Mol. Struct. 470(3) (1998) 241-246.
689 [32] Y. Zhang, Z. Sun, H. Wang, Y. Wang, M. Liang, S. Xue, Nitrogen-doped
690 graphene as a cathode material for dye-sensitized solar cells: effects of
691 hydrothermal reaction and annealing on electrocatalytic performance, RSC Adv.
692 5(14) (2015) 10430-10439.
693 [33] S. Indrawirawan, H. Sun, X. Duan, S. Wang, Low temperature combustion
694 synthesis of nitrogen-doped graphene for metal-free catalytic oxidation, J. Mater.
695 Chem. A 3(7) (2015) 3432-3440.
696 [34] S. Gunasekaran, G. Sankari, S. Ponnusamy, Vibrational spectral investigation on
697 xanthine and its derivatives—theophylline, caffeine and theobromine,
698 Spectrochimica Acta Part A: Molecular and Biomolecular Spectroscopy 61(1-2)
699 (2005) 117-127.
700 [35] G. Wang, L.-T. Jia, Y. Zhu, B. Hou, D.-B. Li, Y.-H. Sun, Novel preparation of
701 nitrogen-doped graphene in various forms with aqueous ammonia under mild
702 conditions, RSC Adv. 2(30) (2012) 11249.
703 [36] J. Liu, H. Wang, M. Antonietti, Graphitic carbon nitride "reloaded": emerging
704 applications beyond (photo)catalysis, Chem. Soc. Rev. 45(8) (2016) 2308-2326.
705 [37] Y. Oaki, S. Kaneko, H. Imai, Morphology and orientation control of guanine
706 crystals: a biogenic architecture and its structure mimetics, J. Mater. Chem. 22(42)
707 (2012) 22686.

[38] L.T. Soo, K.S. Loh, A.B. Mohamad, W.R.W. Daud, The effect of varying N/C ratios of nitrogen precursors during non-metal graphene catalyst synthesis, Int. J. Hydrogen Energy (2016).

[39] T. Horibe, K. Kusaba, K. Niwa, M. Hasegawa, K. Yasuda, R. Ishigami, Molecular routes syntheses of graphite-like C–N compounds with various N/C ratios in high pressure and temperature, J. Ceram. Soc. Jpn. 124(10) (2016) 1013-1016.

[40] A.P. Dementjev, A. de Graaf, M.C.M. van de Sanden, K.I. Maslakov, A.V. Naumkin, A.A. Serov, X-Ray photoelectron spectroscopy reference data for identification of the C3N4 phase in carbon–nitrogen films, Diamond Relat. Mater. 9(11) (2000) 1904-1907.

[41] D. Hulicova-Jurcakova, M. Kodama, S. Shiraishi, H. Hatori, Z.H. Zhu, G.Q. Lu, Nitrogen-Enriched Nonporous Carbon Electrodes with Extraordinary Supercapacitance, Adv. Funct. Mater. 19(11) (2009) 1800-1809.

[42] S. Kundu, T.C. Nagaiah, W. Xia, Y. Wang, S.V. Dommele, J.H. Bitter, et al., Electrocatalytic Activity and Stability of Nitrogen-Containing Carbon Nanotubes in the Oxygen Reduction Reaction, J. Phys. Chem. C 113(32) (2009) 14302-14310.

[43] H. Liu, Y. Zhang, R. Li, X. Sun, S. Désilets, H. Abou-Rachid, et al., Structural and morphological control of aligned nitrogen-doped carbon nanotubes, Carbon 48(5) (2010) 1498-1507.

[44] A. Kumar, A. Ganguly, P. Papakonstantinou, Thermal stability study of nitrogen functionalities in a graphene network, J. Phys.: Condens. Matter 24(23) (2012) 235503.

[45] T. Sharifi, G. Hu, X. Jia, T. Wågberg, Formation of Active Sites for Oxygen Reduction Reactions by Transformation of Nitrogen Functionalities in Nitrogen-

733 Doped Carbon Nanotubes, ACS Nano 6(10) (2012) 8904-8912.

734 [46] M. Scardamaglia, C. Struzzi, S. Osella, N. Reckinger, J.-F. Colomer, L. Petaccia,
735 et al., Tuning nitrogen species to control the charge carrier concentration in highly
736 doped graphene, 2D Materials 3(1) (2016) 011001.

737 [47] P.C. Upadhya, Y.C. Shen, A.G. Davies, E.H. Linfield, J. Biol. Phys. 29(2/3)
738 (2003) 117-121.

739 [48] P. Chamorro-Posada, Study of the terahertz spectra of crystalline materials using
740 NDDO semi-empirical methods: polyethylene, poly (vinylidene fluoride) form II
741 and α-D-glucose, arXiv:1604.03919 [physics.chem-ph] (2016).

742 [49] M.H. Mingxia He, J.H. Jiaguang Han, M.L. Meng Li, Z.T. Zhen Tian, Y.Y.
743 Yanjun Yu, W.Z. Weili Zhang, Terahertz spectroscopy studies of far-infrared
744 optical and dielectric signatures of melamine, Chin. Opt. Lett. 9(s1) (2011)
745 s10507-310509.

746 [50] M. Walther, B.M. Fischer, P. Uhd Jepsen, Noncovalent intermolecular forces in
747 polycrystalline and amorphous saccharides in the far infrared, Chem. Phys. 288(2-
748 3) (2003) 261-268.

749 [51] P. Chamorro-Posada, J. Vázquez-Cabo, Ó. Rubiños-López, J. Martín-Gil, S.
750 Hernández-Navarro, P. Martín-Ramos, et al., THz TDS study of several sp2
751 carbon materials: Graphite, needle coke and graphene oxides, Carbon 98 (2016)
752 484-490.

753 [52] P. Chamorro-Posada, J. Vázquez-Cabo, F.M. Sánchez-Arévalo, P. Martín-Ramos,
754 J. Martín-Gil, L.M. Navas-Gracia, et al., 2D to 3D transition of polymeric carbon
755 nitride nanosheets, J. Solid State Chem. 219 (2014) 232-241.

756 [53] H. Ringertz, The molecular and crystal structure of uric acid, Acta Crystallogr.
757 20(3) (1966) 397-403.

758 [54] C.F. Macrae, P.R. Edgington, P. McCabe, E. Pidcock, G.P. Shields, R. Taylor, et
759 al., Mercury: visualization and analysis of crystal structures, J. Appl. Crystallogr.
760 39(3) (2006) 453-457.
761 [55] J.J.P. Stewart, Application of the PM6 method to modeling the solid state, J. Mol.
762 Model. 14(6) (2008) 499-535.
763 [56] P. Chamorro-Posada, I. Silva-Castro, J. Vázquez-Cabo, P. Martín-Ramos, J.M.
764 López-Santos, J. Martín-Gil, A Study of the Far Infrared Spectrum of N-Acetyl-D-
765 Glucosamine Using THz-TDS, FTIR, and Semiempirical Quantum Chemistry
766 Methods, J. Spectrosc. 2016 (2016) 1-7.
767 [57] A.-R. Allouche, Gabedit-A graphical user interface for computational chemistry
768 softwares, J. Comput. Chem. 32(1) (2011) 174-182.
769 [58] D.-K. Seo, R. Hoffmann, Direct and indirect band gap types in one-dimensional
770 conjugated or stacked organic materials, Theor. Chem. Acc. 102(1-6) (1999) 23-
771 32.
772 [59] J. Ridley, M. Zerner, An intermediate neglect of differential overlap technique for
773 spectroscopy: Pyrrole and the azines, Theor. Chim. Acta 32(2) (1973) 111-134.
774 [60] P.M. Lahti, J. Obrzut, F.E. Karasz, Use of the Pariser-Parr-Pople approximation to
775 obtain practically useful predictions for electronic spectral properties of
776 conducting polymers, Macromolecules 20(8) (1987) 2023-2026.
777 [61] M.C. Zerner, G.H. Loew, R.F. Kirchner, U.T. Mueller-Westerhoff, An
778 intermediate neglect of differential overlap technique for spectroscopy of
779 transition-metal complexes. Ferrocene, J. Am. Chem. Soc. 102(2) (1980) 589-599.
780 [62] F. Neese, The ORCA program system, Wiley Interdiscip. Rev.: Comput. Mol. Sci.
781 2(1) (2012) 73-78.

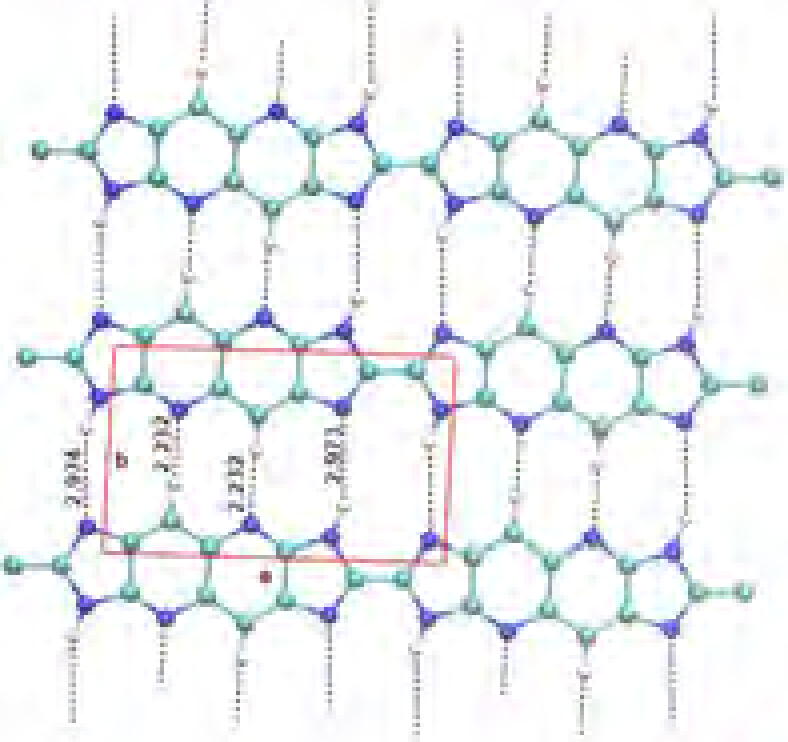

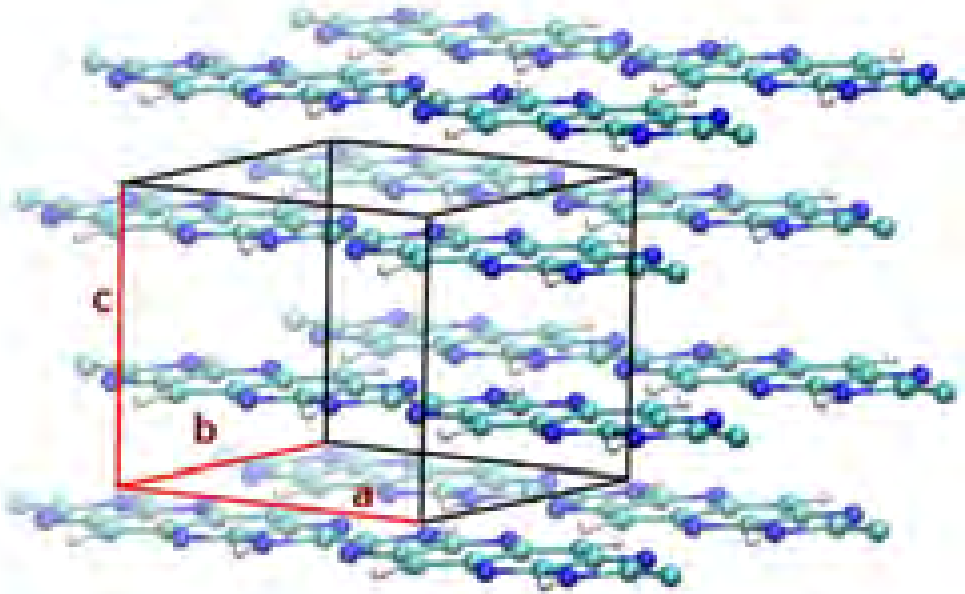

$$2nC_5H_4N_4O_3 \rightarrow (C_{10}N_6H_4)_n + 2nH_2O + 2nNO_2$$